ARTICLE IN PRESS

Ceramics International xxx (xxxx) xxx

Contents lists available at ScienceDirect

Ceramics International

journal homepage: www.elsevier.com/locate/ceramint

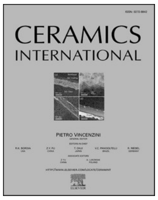

Characterization of high-temperature compressive behaviour of field-assisted sintered niobium-alumina refractory composites

Gökhan Günay [a,b,*], Gregory Kallien [c], Bastian Kraft [c], Susanne Wagner [c], Karl Günter Schell [c], Martin Heilmaier [d], Horst Biermann [a,b], Anja Weidner [a,b]

[a] *Institute of Materials Engineering, Technische Universität Bergakademie Freiberg, Gustav-Zeuner-Str. 5, 09599, Freiberg, Germany*
[b] *Center for Efficient High Temperature Processes and Materials Conversion, Technische Universität Bergakademie Freiberg, Winklerstr. 5, 09599, Freiberg, Germany*
[c] *IAM – Ceramic Materials and Technologies, Karlsruhe Institute of Technology (KIT), Hain-und-Neu-Str. 7, 76131, Karlsruhe, Germany*
[d] *IAM – Werkstoffkunde (IAM-WK), Karlsruhe Institute of Technology (KIT), Kaiserstraße 12, 76131, Karlsruhe, Germany*

ARTICLE INFO

Keywords:
Refractory composites
Field-assisted sintering
Mechanical properties
Particle size

ABSTRACT

Nb-Al_2O_3 refractory composites have attracted significant attention due to their excellent performance at elevated temperatures. The incorporation of both metallic (Nb) and ceramic (Al_2O_3) phases enhances interest in these materials, i.e., the combination of the high toughness and plasticity of niobium with the refractoriness, high hardness, thermal stability, and oxidation resistance of alumina. In this study, the high-temperature mechanical behaviour of Nb-Al_2O_3 composites produced via field-assisted sintering (FAST) was investigated under compressive loading. Composites containing alumina particles of different sizes were subjected to compressive tests up to 1350 °C. The results were evaluated with respect to Nb content, alumina particle size, applied stress, and test temperature. Initial and post-mortem microstructural analyses were carried out to characterise the deformation behaviour. It was observed that an increase in the metal content led to an enhancement of plasticity, while changes in alumina particle size influenced the deformation behaviour.

1. Introduction

Nb-Al_2O_3 refractory composites have gained considerable attention due to their remarkable high-temperature properties. Nb and Al_2O_3, having similar coefficients of thermal expansion (CTE) [1–5], impart their inherent characteristics to these composites, enabling excellent thermal and electrical conductivity, superior creep and corrosion resistance at elevated temperatures, and enhanced toughness [6,7]. When produced with a coarse-grained microstructure, these materials exhibit good thermal shock resistance, low shrinkage during sintering, and strong creep performance, making them highly promising candidates for manufacturing technologies exposed to extreme thermal and environmental conditions [8–11]. At the same time, the long-term integrity of such composites critically depends on the stability of the ceramic–metal interface [12].

Previous studies by the authors on vibration-assisted casting and extrusion routes for Nb-Al_2O_3 composites have shown that porosity plays a decisive role in governing the mechanical performance of these composites [13,14]. This strong influence of porosity on mechanical behaviour is also well established in the broader literature on metal–ceramic composites [13–16]. One of the key methods to reduce porosity and achieve a dense structure with enhanced electrical conductivity is the field-assisted sintering technology (FAST), which enables high densification with minimal grain growth and without binders owing to its rapid heating and applied uniaxial pressure within graphite dies [17,18]. However, the FAST is not suitable to manufacture large-scale components for industrial applications. At industrial scale, cold isostatic pressing (CIP) is widely used to shape ceramic and metal-based composites, but requires additional sintering, which may cause grain growth and porosity retention. In contrast, FAST allows well-controlled, rapid densification in laboratory studies, enabling fine-grained microstructures and improved mechanical performance.

Several investigations have been conducted on Nb-Al_2O_3 composites synthesised via FAST. De la Torre et al. [19] studied the fabrication of Nb-Al_2O_3 refractory composites containing 50 vol% Nb using FAST, successfully increasing their density without altering the grain size. Hardness measurements and room temperature (RT) bending test results confirmed that denser materials exhibited higher hardness and bending

---

[*] Corresponding author. TU Bergakademie Freiberg, Institut für Werkstofftechnik, Gustav-Zeuner-Str. 5, 09599, Freiberg, Germany.
E-mail address: goekhan.guenay@iwt.tu-freiberg.de (G. Günay).

https://doi.org/10.1016/j.ceramint.2026.03.228
Received 23 September 2025; Received in revised form 10 March 2026; Accepted 15 March 2026

Please cite this article as: Gökhan Günay et al., *Ceramics International*, https://doi.org/10.1016/j.ceramint.2026.03.228

strength. Saucedo-Acuña et al. [20] examined the sulfidation and oxidation behaviour of Nb-Al_2O_3 composites at 900 °C, identifying new phases that formed under severe oxidation conditions. Dotta et al. [21] investigated the fracture and tribological behaviour of FAST-processed Nb-Al_2O_3 composites with 15, 25, and 35 vol% Nb using the Vickers-indentation based fracture toughness measurements at RT. Kraft et al. [22] investigated the effect of particle size on the microstructural and electrical properties of Nb-Al_2O_3 composites produced with alumina powders of different particle sizes and different Nb contents. The results indicated that composites fabricated with smaller alumina particles achieved higher density, while an increase in Nb content enhanced electrical conductivity; moreover, coarser alumina particles were found to further enhance conductivity and reduce the percolation threshold.

Nb-Al_2O_3 refractory composites are known to be used in high-temperature and harsh environments, where they are subjected to substantial mechanical loads. Given their low porosity, an improvement in mechanical properties is expected. However, despite the existing literature, no studies have addressed their high-temperature behaviour after FAST processing for high densification. Moreover, indentation-based fracture toughness approaches are prone to limitations in metal–ceramic composites with restricted plasticity [21]. Recent work has, therefore, applied fracture-mechanics-based characterisation (e.g., R-curve and subcritical crack-growth sensitivity) to Nb–Al_2O_3 systems at room temperature [23]. Nevertheless, elevated-temperature mechanical data remain scarce. Understanding their high-temperature mechanical behaviour is essential for broadening their potential application areas.

In the present study, Nb–Al_2O_3 refractory composites with different alumina particle sizes and niobium contents were produced via FAST and subjected to quasi-static compression and static creep experiments up to 1350 °C, covering the temperature range relevant for potential high-temperature applications. The results were analysed with respect to the effects of alumina particle size, test temperature, niobium content, and applied stress. Microstructural characterisation was performed prior to and after mechanical testing to shed light on the acting deformation mechanisms. This study represents the first comprehensive investigation of the high-temperature mechanical properties of Nb–Al_2O_3 composites produced via FAST.

2. Experimental procedures

2.1. Materials

In the current study, materials were produced using the FAST method. The production process employed niobium powder (EWG Wagner, Germany) together with two alumina powders of different particle sizes (CT9FG, Almatis, Germany; Alodur WRG, Imerys Fused Minerals Zschornewitz, Germany). The particle sizes, purities and main impurities of the raw materials are summarised in Table 1. In this process, the raw material powders were first homogenized for 10 min using a T2C-type turbular tumbler (WAB AG Maschinenfabrik, Switzerland). No binder was added during this stage. Subsequently, the powder mixture was dried and placed into graphite plates suitable for the sintering process. The prepared mixture was then positioned inside an HP D 25/1 system (FCT Systeme GmbH, Germany) for sintering. Before sintering, the system was heated to 1600 °C at a rate of 50 K min^{-1}. Once this temperature was reached, the material was sintered under vacuum (∼10 mbar) in an argon atmosphere while applying an axial pressure of 50 MPa for 5 min. After sintering, the composite was cooled at the same rate of 50 K min^{-1}. The single-phase niobium materials were manufactured accordingly. For further details, refer to Kraft et al. [22].

Table 1
Particle sizes distributions, purities and main impurities of the raw materials.

Raw materials	Particle Size [µm]			Purity	Main Impurities [wt. %]
	d_{10}	d_{50}	d_{90}		
Niobium	10.8	37.6	78.6	99.9 wt% Nb	O: 0.3, C: 0.04, Ta: 0.05
Alodur	44.8	95.8	162.3	99.7 wt% Al_2O_3	Na: 0.3, Si: 0.02, Fe: 0.01
CT9FG	0.8	4.4	11.9	99.5 wt% Al_2O_3	Na: 0.1, Si: 0.03, Ca: 0.03

Following the sintering process, discs with a diameter of 40 mm and a maximum height of 6 mm were obtained. Due to the small size of the final test specimens, porosity and density measurements were conducted for the entire discs using the Archimedes method. For the calculation of relative density, theoretical densities of 8.57 g/cm^3 for Nb [24] and 3.95 g/cm^3 for α-corundum [25] were used. After the measurements were completed, cylindrical specimens with a diameter of 2.5 – 6.2 mm and a height of 2.6 – 6.3 mm were prepared using water-jet cutting (Atech GmbH, Germany).

For mechanical testing, Nb–Al_2O_3 composites were manufactured with Nb/Al_2O_3 volume ratios of 20/80, 40/60, 60/40, and 80/20 (vol %). The materials were classified based on the type of alumina powder used (CT9FG or Alodur) and referred to as Nb/CT9FG and Nb/Alodur. Additionally, the single-phase niobium material (100 Nb) was tested as a reference material.

2.2. Mechanical testing

In order to characterise the high-temperature mechanical properties of Nb-Al_2O_3 refractory composites, quasi-static compression as well as creep tests were conducted under uniaxial compressive loading at high temperatures up to 1350 °C. The experiments were performed using an electromechanical testing machine (Z020, Zwick Roell, Germany) with an integrated water-cooled chamber (Maytec, Germany) to ensure isolation from environmental conditions. Specimens were heated by means of a medium-frequency induction heating generator (TruHeat HF 5010, Trumpf Hüttinger GmbH, Germany) at a heating rate of 30 K min^{-1} using a water-cooled copper induction coil. Throughout the entire testing process, temperature control was maintained using a pyrometer (Sensotherm Metis MS09, Germany), which recorded data directly from the specimen surface with an emissivity of 0.93. Prior to each test, the chamber was evacuated twice to a pressure of 0.7 mbar and subsequently purged with argon gas to remove residual oxygen. All experiments were carried out under argon atmosphere to prevent oxidation, and the oxygen level was continuously monitored using an oxygen sensor (Stange Elektronik, Germany).

To ensure uniform temperature distribution throughout the specimens, they were positioned between TZM (titanium-zirconium-molybdenum) alloy susceptors and enclosed within a TZM cage. Once mounted, the lower piston was advanced at 0.1 mm min^{-1} to apply a 5 N preload, seating the specimen and eliminating initial machine compliance and fixture slack. Prior to each mechanical test, the specimens were held under preload at the target testing temperature for 5 min to ensure thermal stability.

Quasi-static compression tests were performed at an initial strain rate of $7.5 \times 10^{-4}\ s^{-1}$ at 1300 °C. To assess experimental scatter, the 60/40 Nb/CT9FG composites were tested three times, whereas the 60/40 Nb/Alodur composites were tested five times. As the present study primarily focuses on the 60/40 composite systems, the remaining compositions were each tested once. Since the post-yield response may be influenced by factors such as friction and the very small specimen dimensions, the stress–strain curves are plotted with dashed lines beyond 10% strain to indicate this increased uncertainty.

Creep experiments were conducted at 1250, 1300, and 1350 °C at constant forces under initial stresses of 40, 50, and 70 MPa for durations of up to 9 h. However, some tests were terminated earlier, between 6 and 8 h, due to limitations in the strain measurement capability of the testing system, which is influenced by both specimen geometry and equipment constraints and is typically ∼40%. Since changes in specimen diameter could not be monitored during the experiments, the applied stresses were calculated based on the initial cross-sectional areas, and the corresponding force values were kept constant throughout the tests. As a consequence, a significant decrease in the strain rate values was observed beyond a certain point in the creep curves under constant force, which is attributed to diameter variations during deformation. This reduction was detected at different strain levels for each specimen depending on the test conditions, but it occurred not earlier than approximately 10% strain. Therefore, these segments are represented by dashed lines beyond the 10% strain mark in all creep curves.

2.3. Microstructural characterization

In order to rationalise the deformation behaviour and the damage of the materials, the microstructures of the test specimens were examined both prior to and after mechanical tests. For this purpose, the specimens were prepared using standard metallographic techniques. Initially, the specimens were sectioned parallel to the compression/loading direction and embedded in conductive resin. The surface preparation of the specimens was carried out through a sequential grinding and polishing procedure. Initially, the specimens were ground with a 70 μm diamond disc down to 22 μm. This was followed by lapping with diamond abrasives down to 6 μm. Subsequently, the specimens were polished with a 1 μm diamond suspension, and then oxide polishing was performed using 0.25 μm Al_2O_3 suspension. Finally, the specimens underwent 24 h of vibratory polishing to achieve a high-quality surface finish suitable for microstructural analysis.

Microstructural examinations were performed using a high-resolution field-emission scanning electron microscope (SEM) (Mira 3 XMU, Tescan, Czech Republic). Changes in morphological features and phase distributions were analysed using both secondary electron (SE) and back-scattered electron (BSE) contrast imaging modes.

In addition, electron backscatter diffraction (EBSD) scans were performed on the Nb/CT9FG and Nb/Alodur composites containing 60 vol % niobium, both in the as-sintered state and after mechanical testing to evaluate the phase composition, average grain size, grain orientation, crystallographic texture, and kernel average misorientation (KAM). Before the measurements, the surfaces of the specimens were coated with a thin platinum layer to avoid charging effects. The measurements were conducted for an area of interest of 250 μm × 200 μm at an acceleration voltage of 20 kV and a step size of 0.2 μm, employing the APEXsuite data acquisition and analysis software (EDAX, Ametek, USA). Kikuchi patterns were acquired using 8 × 8 binning, with an acquisition time range of 0.1–100 ms. The average area weighted grain size was evaluated using a misorientation angle of 12°. Grains cutting the edge of the EBSD map were excluded from the grain size evaluation. Furthermore, low-angle grain boundaries (LAGBs) and high-angle grain boundaries (HAGB) were evaluated with misorientation angles of 2° to 12° and >12°, respectively. Kernal average misorientation was calculated considering the 4th nearest neighbours of each measuring point and were displayed in a misorientation angle range between 0° and 3°.

3. Results

3.1. Initial microstructures

The initial microstructures of the compositions containing CT9FG and Alodur alumina powders are shown in Fig. 1, exemplified by the 60/40 composition. Since the majority of the mechanical tests were performed on 60/40 Nb-Al_2O_3 composites, microstructural analyses were focused on this composition.

In both composites, the dark regions correspond to Al_2O_3, while the light grey areas represent Nb particles. These Al_2O_3 and Nb particles are uniformly distributed throughout the microstructure.

A clear difference was observed in the particle sizes of the CT9FG and Alodur alumina powders. In the composites containing CT9FG, Nb particles appeared more isolated surrounded by the Al_2O_3 phase, whereas in the Alodur-containing composites, metallic continuity was more evident. This morphology can be attributed to the lower surface area of the larger Alodur particles, which reduced their interaction with Nb and, consequently, promoted the interconnection and clustering of niobium particles during FAST processing.

In addition, EBSD scans were performed as an example for 60/40 Nb/CT9FG and Nb/Alodur FAST materials to study both the grain sizes and crystallographic orientations of both phases: niobium and alumina. For the 60/40 Nb/CT9FG composite, Fig. 2 shows the band contrast map (a), the phase map (b) and crystallographic orientation maps of niobium (c, d) and alumina (e, f) with respect to the surface normal (c, e) and the loading axis (d, f). The loading axis was parallel to the pressure direction during FAST. The average area weighted grain sizes evaluated from EBSD measurements on the Nb/CT9FG composites is with 22 μm ± 16 μm and 5 μm ± 2 μm for niobium and alumina, respectively, a bit less for niobium and in the same order of magnitude for alumina than the d_{50} values of the powder particle size distributions as shown in Table 1.

For the 60/40 Nb/Alodur composite, Fig. 3 shows the EBSD results in terms of band contrast map (a), phase map (b) and crystallographic orientation maps of niobium (c) and Alodur (d) with respect to the loading axis. As it is evident, the particle size of Alodur is significantly higher compared to CT9FG shown in Fig. 2.

3.2. Porosity and density

Table 2 presents the density and porosity values of the Nb-Al_2O_3 composite discs measured using the Archimedes method. According to these results, the bulk density values of the Nb/CT9FG composites are relatively higher than those of the Nb/Alodur composites.

With respect to porosity, the most notable value belongs to the 20/80 Nb/Alodur composite, which exhibited a porosity of 7.7%, whereas the open porosity of all other composites remained below 1.2%. Although the bulk density of the composites increased with increasing Nb content, no significant differences were observed in their porosity values. The markedly higher porosity of the 20/80 Nb/Alodur composite compared

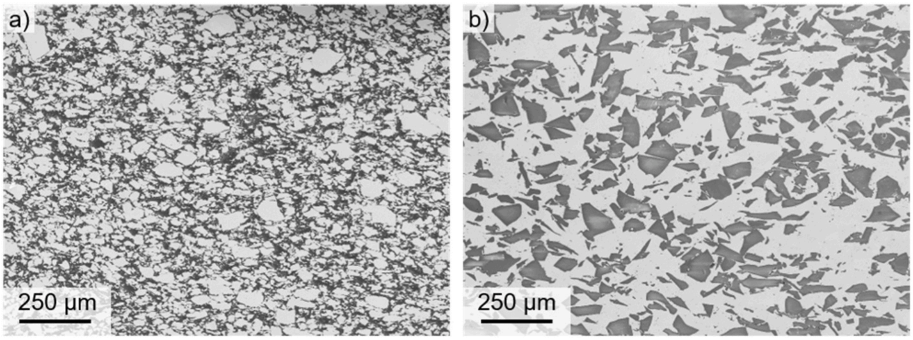

Fig. 1. SEM micrographs of 60/40 Nb-Al_2O_3 composites containing CT9FG (a) and Alodur (b) captured in secondary electron contrast. Pressure direction during FAST is vertical.

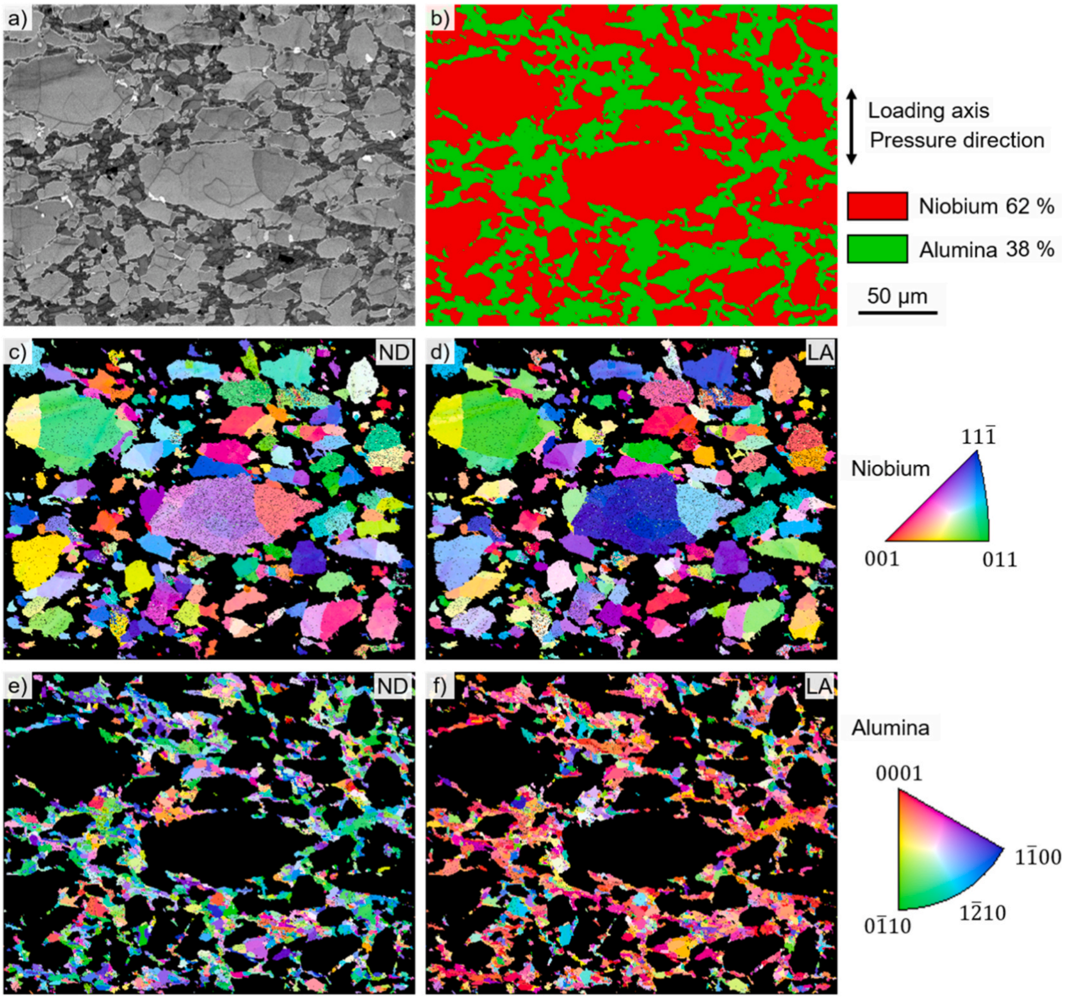

Fig. 2. Results of EBSD measurement on 60/40 Nb/CT9FG composite. (a) Band contrast map. (b) Phase map. Red – niobium, green – alumina. (c, d) Crystallographic orientation of niobium with respect to the normal direction (ND) in (c) and loading axis (LA) in (d). (e, f) Crystallographic orientation of alumina with respect to the normal direction (ND) in (e) and loading axis (LA) in (f). Loading axis is vertical in the figure and parallel to the pressure direction during FAST. Grains cutting the edge of the EBSD map were excluded from the grain size evaluation. (For interpretation of the references to colour in this figure legend, the reader is referred to the Web version of this article.)

to the other compositions can be primarily attributed to the difference in alumina particle size. The coarser Alodur particles result in less efficient particle packing and reduced ceramic–metal interfacial contact during FAST processing, which limits pore elimination under otherwise identical processing conditions. In contrast, the finer CT9FG alumina promotes improved initial packing density and facilitates a more homogeneous distribution of stress and electric current during FAST, thereby enhancing densification and leading to lower residual porosity.

When the relative density results are evaluated in relation to the particle size data provided in Table 1, the influence of the raw material particle size on the relative density of the composites becomes evident. Despite having low porosity values, the Nb/CT9FG composites, which contain finer particles compared to Nb/Alodur and the fully Nb-based reference, exhibited higher relative densities.

3.3. Mechanical behaviour

Fig. 4 presents the results of the quasi-static compression tests conducted at 1300 °C on composites with different compositions using CT9FG (a) and Alodur (b) alumina powders. For both composite types, an increase in Nb content led to more pronounced plastic deformation [3]. Conversely, increasing the Al_2O_3 content reduced plasticity, and the specimens failed at lower strain levels. As shown in Fig. 4a, the Nb/CT9FG composites containing 20% and 40% Nb failed shortly after reaching their maximum compressive strength at only limited strain. The composite with 60% Nb failed after exhibiting more than 20% strain, whereas the one with 80% Nb completed the test without failure, showing a steady flow stress of about 100 MPa. In Fig. 4b, the Nb/Alodur composites displayed different behaviour: the specimen with 20% Nb failed after reaching its maximum compressive strength at ~12% strain, while the other specimens did not fail within the tested strain range and completed the tests by exhibiting increasing stress with increasing strain.

Fig. 4c shows the variations in yield strength (R_{p1}) of composites with alumina particle sizes as a function of Nb content. The R_{p1} value was selected as the yield strength parameter, since initial system compliance effects occurred prior to the full load transfer to the specimen. By excluding this segment, R_{p1} provided a more consistent and comparable measure of yield strength for all specimens. For the 60/40 compositions, which were tested repeatedly to assess scatter, the Nb/CT9FG composites exhibited a yield strength of 145 ± 11 MPa, whereas the Nb/Alodur composites showed 103 ± 24 MPa; the corresponding standard deviations are presented as error bars in Fig. 4c.

It was observed that Nb/Alodur composites, which contain larger alumina particles, exhibited higher yield strength at 20% and 40% Nb content, whereas those with 60% and 80% Nb content showed lower

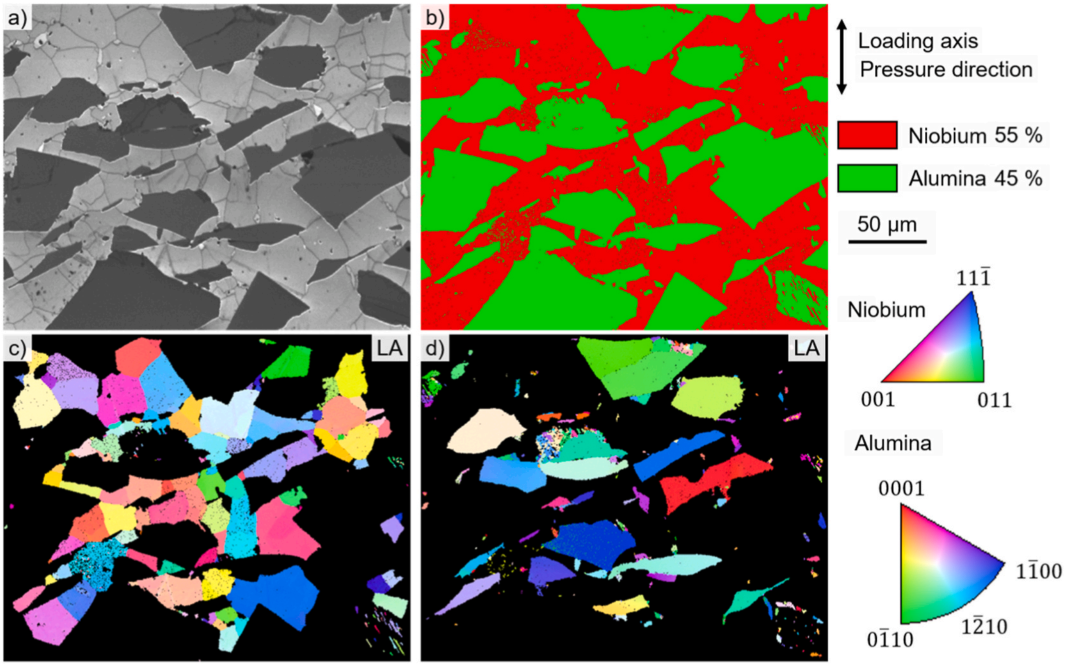

Fig. 3. Results of EBSD measurement on 60/40 Nb/Alodur composite. (a) Band contrast map. (b) Phase map. Red – niobium, green – alumina. (c, d) Crystallographic orientation of niobium and alumina with respect to the loading axis (LA) in (c, d). Loading axis is vertical in the figure and parallel to the pressure direction during FAST. Grains cutting the edge of the EBSD map were excluded from the grain size evaluation. (For interpretation of the references to colour in this figure legend, the reader is referred to the Web version of this article.)

Table 2
Measured bulk density, open porosity and relative density values of the composites.

Composite	Composition	Bulk density (ρ_b)	Open porosity (π_a)	Relative density
		g/cm^3	%	-
Nb/ CT9FG	20/80	4.9	0.8	0.99
	40/60	5.8	0.6	1.00
	60/40	6.7	0.7	0.99
	80/20	7.6	0.9	0.99
Nb/ Alodur	20/80	4.3	7.7	0.90
	40/60	5.5	1.2	0.94
	60/40	6.6	0.6	0.96
	80/20	7.6	0.6	0.99
Reference	100 Nb	8.1	1.3	0.96

yield strength than the Nb/CT9FG composites. Moreover, Nb/CT9FG composites followed a linear rule of mixture with respect to the fraction of Nb, as shown in Fig. 4c. However, a similar trend was not observed for Nb/Alodur composites. These findings underscore the influence of both the ceramic phase fraction and the raw material particle size on the mechanical properties. Overall, a general decrease in yield strength with increasing niobium content was evident.

3.4. *Creep*

Figs. 5–7 present the results of creep tests performed on Nb–Al_2O_3 composites. Fig. 5 presents the creep test results of the 60/40 Nb/CT9FG composites conducted at 1300 °C under initial stresses of 40, 50, and 70 MPa (Fig. 5a and b), as well as at temperatures of 1250, 1300, and 1350 °C under an initial stress of 50 MPa (Fig. 5c and d). At constant temperature, increasing the applied stress led to a noticeable reduction in creep resistance, resulting in faster deformation. Among the stress-dependent tests (Fig. 5a and b), the specimen tested under an initial load of 70 MPa exhibited the highest creep deformation, reaching approximately 24% strain after 6 h. In contrast, the specimens tested at 40 MPa and 50 MPa showed significantly lower creep rates, with final strains of approximately 8% and 12%, respectively, after a 9-h test duration. In the specimen tested at 40 MPa, a distinct behaviour was observed compared to the other specimens. After reaching the minimum strain rate during the test, the strain rate subsequently increased and continued to rise for the remainder of the experiment. This behaviour is believed to be related to certain microstructural factors within the specimen that may have facilitated accelerated deformation at later stages of testing. Possible explanations include the progressive fracture of small alumina particles, partial debonding at Nb/Al_2O_3 interfaces, or the nucleation of voids and cavities. These microstructural changes may have reduced the local resistance against deformation, thereby contributing to the observed increase in strain rate.

A trend similar to stress-dependent tests was observed in the temperature-dependent tests (Fig. 5c and d). As the temperature increased, the materials exhibited reduced creep resistance, accompanied by higher creep rates and strains. The specimen tested at 1350 °C reached a final strain of approximately 33%, whereas those tested at 1300 °C and 1250 °C showed final strains of approximately 12% and 5%, respectively, after 9 h. The contrast in behaviour between the tests at 1300 °C and 1350 °C was particularly notable, with the latter exhibiting a markedly higher creep rate. These findings highlight the pronounced influence of both temperature and applied stress on the creep performance of the composites. A similar behaviour to that observed in the specimen tested at 1300 °C at 40 MPa was also recorded in the specimen tested at 1250 °C and 50 MPa. After reaching the minimum strain rate, the specimen exhibited a subsequent increase in strain rate, continuing until the end of the experiment. As in the previous case, this phenomenon is believed to be influenced by microstructural factors that may have promoted localised deformation at the later stages of creep.

To study the influence of the niobium content on the creep behaviour, Fig. 6 presents the creep test results of Nb/CT9FG composites with 40%, 60%, and 80% Nb, tested at an initial stress of 50 MPa. As shown in the figure, an increase in niobium content led to enhanced deformation accompanied by higher creep rates. The 80/20 composite exhibited the highest creep strain (~35%), whereas the 40/60 composite showed a

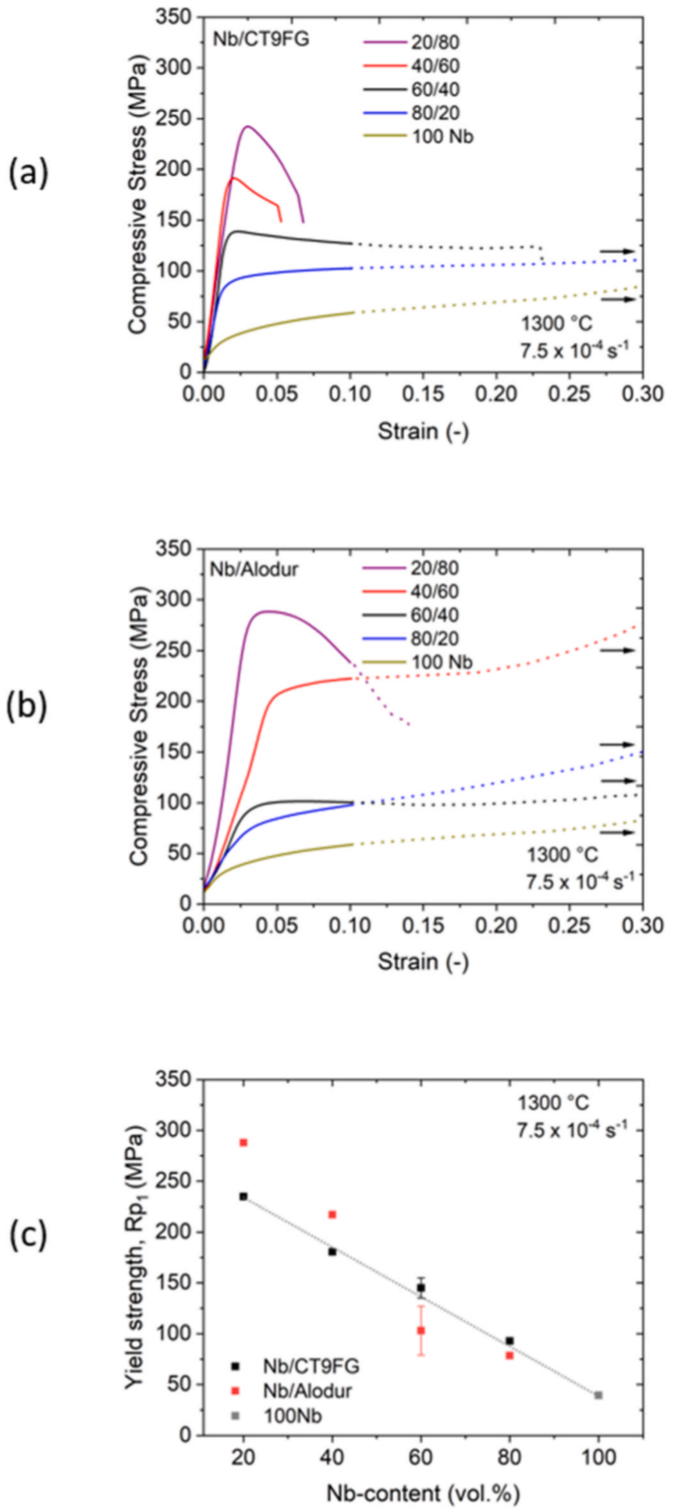

Fig. 4. Compression test results: (a) Nb/CT9FG, (b) Nb/Alodur, (c) variation of yield strength of the composites (R_{p1}) plotted vs. Nb content.

strain of only ~6% due to the higher Al_2O_3 content. Notably, the difference in strain becomes much more pronounced between 60% and 80% Nb, while the variation between 40% and 60% remains comparatively modest.

Fig. 7 presents the creep results of the 60/40 Nb/Alodur composites conducted at a constant temperature of 1300 °C under three different initial stresses (Fig. 7a and b) and at a fixed initial stress of 40 MPa across three temperatures (Fig. 7c and d).

According to the results presented in Fig. 7, the Nb/Alodur composites exhibited creep behaviour comparable to that of the Nb/CT9FG composites. With increasing applied stress, the creep resistance of the composites decreased. The highest creep rate was observed in the specimen tested at 70 MPa, which underwent rapid deformation up to approximately 25% strain, after which the creep rate declined. By the end of the 8-h test, this specimen had reached a total strain of about 35%. In contrast, the other specimens deformed at substantially lower creep rates, with the lowest strain (~7.5%) recorded in the specimen tested at 40 MPa for 9 h. Similar to the Nb/CT9FG composites, this specimen also showed an increase in strain rate during the test. These results further suggest that comparable microstructural factors may be governing the creep behaviour of both composite types.

Similarly, the effect of temperature on creep behaviour (Fig. 7c and d) followed a trend comparable to that observed for the Nb/CT9FG composites. With increasing temperature, the composites exhibited lower creep resistance, with the highest creep deformation occurring in the specimen tested at 1350 °C, which reached a strain of approximately 17%. Conversely, decreasing the temperature led to reduced creep rates, and the lowest creep strain (~2.5%) was recorded after 9 h in the specimen tested at 1250 °C.

The creep behaviour of both Nb/CT9FG and Nb/Alodur composites was analysed using Norton and Arrhenius plots to determine the apparent stress exponent (n_{app}) and the apparent activation energy (Q_{app}), respectively, as shown in Fig. 8. As the investigated materials are multiphase composites, their creep response is governed by the combined effects of several deformation and diffusion mechanisms operating simultaneously within the Nb and Al_2O_3 phases, as well as at their interfaces. Consequently, the experimentally determined stress exponent (n) and activation energy (Q) do not represent intrinsic values of a single-phase material, but rather apparent parameters (n_{app}, Q_{app}) that reflect the overall composite behaviour.

The relationship between stress, temperature, and creep rate was described by the Mukherjee-Bird-Dorn (MBD) creep equation [26]:

$$\dot{\varepsilon} = A \cdot \sigma^{n_{app}} \exp\left(-\frac{Q_{app}}{RT}\right) \tag{1}$$

where $\dot{\varepsilon}$ is the creep rate (s^{-1}), σ is the applied stress (MPa), A is a material dependent parameter, n_{app} is the apparent Norton stress exponent, Q_{app} is the apparent activation energy for creep (kJ/mol), R is the universal gas constant, and T is the absolute temperature in Kelvin. In this study, the value of $R = 8.314$ J/mol·K was used for all calculations.

For the determination of the apparent stress exponent (n_{app}), creep rates at 1%, 1.5%, 2%, and 2.5% strain levels ($\dot{\varepsilon}_{1-2.5}$%) were extracted under constant stresses of 40 MPa, 50 MPa and 70 MPa. Norton plots were constructed based on Equation (1) by plotting log $\dot{\varepsilon}$ versus log σ, and the slopes of these linear fits were taken as the apparent stress exponents. The final values were obtained by averaging across the selected strain levels, and the corresponding deviations are shown as variation bars in the graphs. Based on the 6 to 9 h creep tests, n_{app} was determined as 3 ± 0.2 for Nb/CT9FG and 6.8 ± 0.1 for Nb/Alodur (Fig. 8a). A higher variation in the creep rate data was observed for the Nb/Alodur composites.

Similarly, creep tests conducted at three different temperatures were used to calculate the apparent activation energies of the composites based on Equation (1), and the corresponding Arrhenius plots were generated (Fig. 8b). For each temperature, the creep rates determined at strain levels of 1%, 1.5%, 2%, and 2.5% were considered. The slopes of the Arrhenius plots (ln $\dot{\varepsilon}$ vs. 1/T) were determined for each strain level, and the average slope was used to obtain the mean apparent activation energy together with its deviation. The variations in the logarithmic values of the creep rates at these strain levels are indicated by variation bars, where the upper limits correspond to the values at 1% strain and the lower limits to those at 2.5% strain. As a result of these calculations, the apparent activation energies were determined as 520 ± 57 kJ/mol

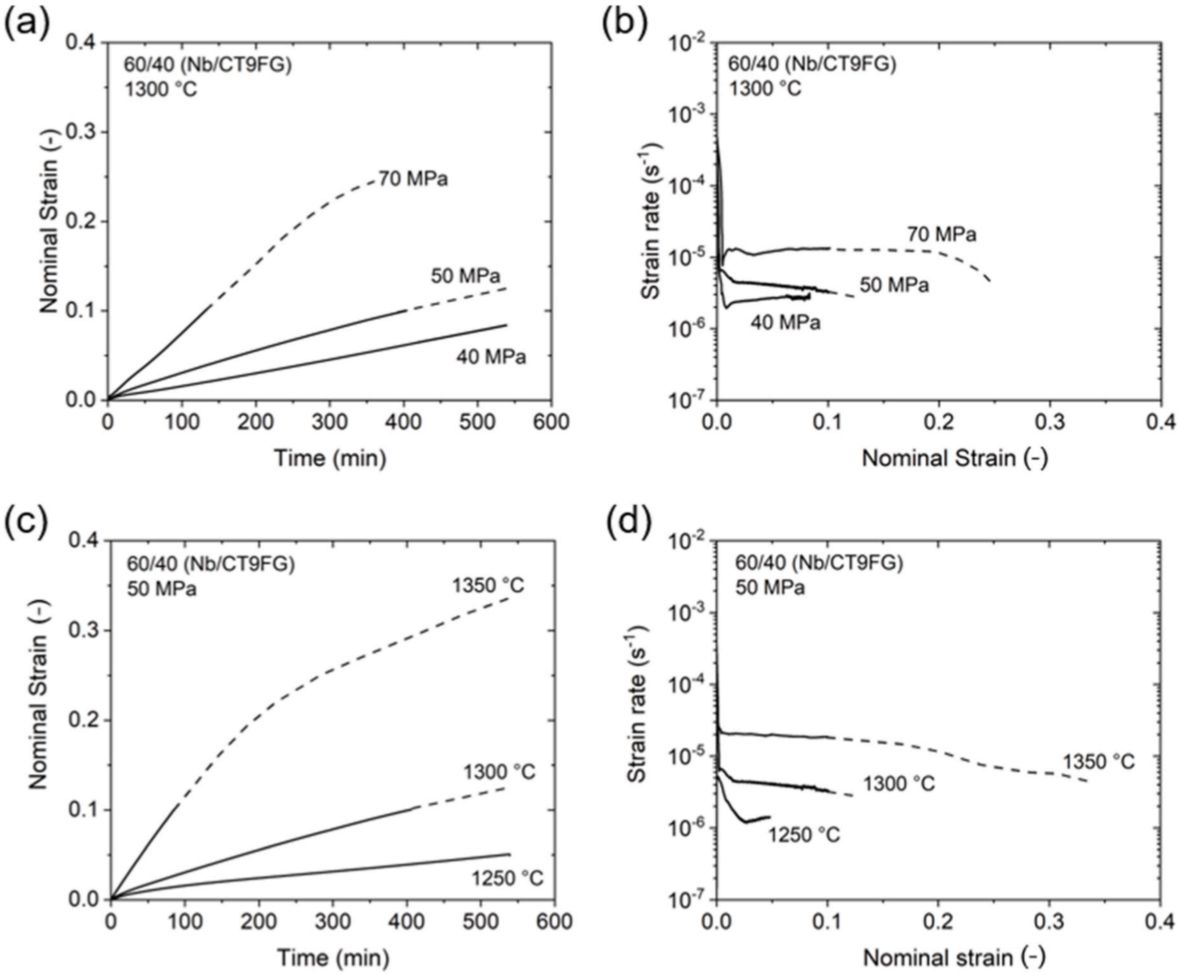

Fig. 5. Creep test results of 60/40 Nb/CT9FG composites: (a, b) tested at 1300 °C at initial stresses of 40, 50, and 70 MPa; (c, d) tested at 50 MPa and temperatures of 1250, 1300, and 1350 °C. Plots show nominal strain vs. time (a, c) and strain rate vs. nominal strain (b, d), respectively.

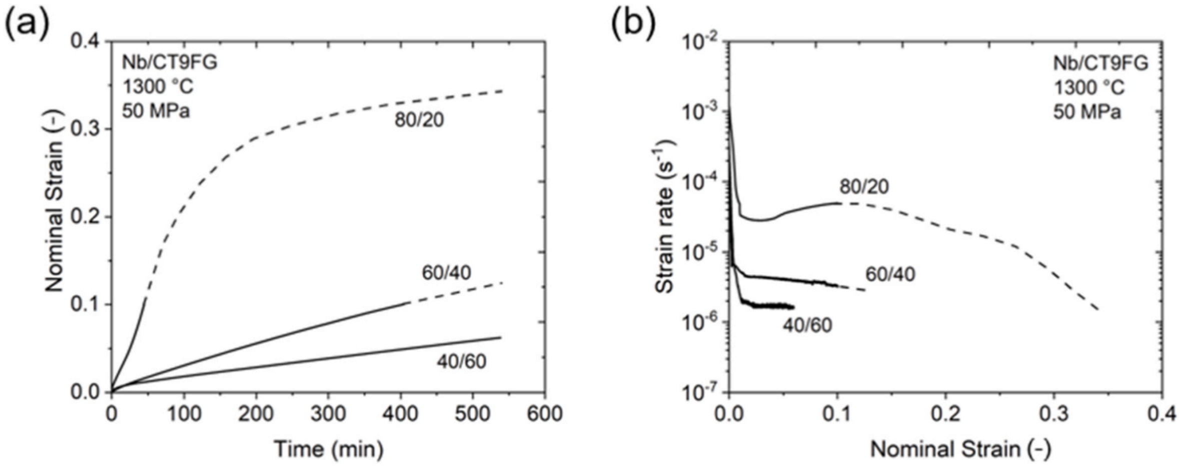

Fig. 6. Creep test results of 40/60, 60/40 and 80/20 Nb/CT9FG composites tested at 1300 °C and an initial stress of 50 MPa: (a) nominal strain vs. time and (b) strain rate vs. nominal strain.

for Nb/CT9FG and 576 ± 41 kJ/mol for Nb/Alodur. These results indicate that both composites exhibited comparable activation energy values. Examination of the variation bars reveals that the Nb/Alodur composite exhibited a higher scatter, whereas for both composites this variation decreased with an increase in temperature.

3.5. *Microstructure of deformed states*

Quasi-static compression. Fig. 9 presents SE micrographs taken from the 60/40 Nb/CT9FG composite after a quasi-static compression test conducted at 1300 °C. While Fig. 9a shows the general overview of the entire specimen after the test, Fig. 9b, c shows areas at higher

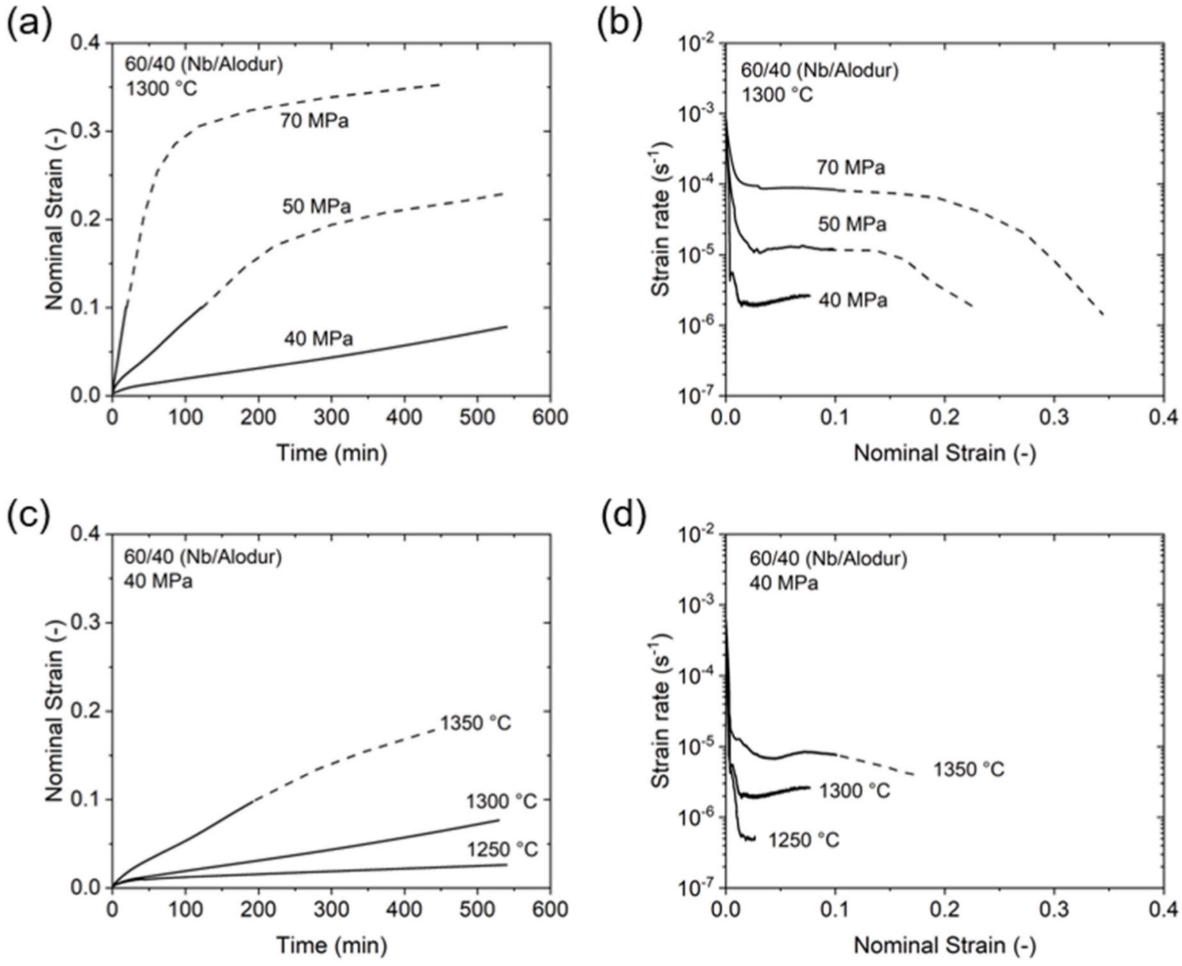

Fig. 7. Creep test results of 60/40 Nb/Alodur composites: (a, b) tested at 1300 °C at initial stresses of 40, 50, and 70 MPa; (c, d) tested at initial stress of 40 MPa at temperatures of 1250, 1300, and 1350 °C. Plots show nominal strain vs. time (a, c) and strain rate vs. nominal strain (b, d), respectively.

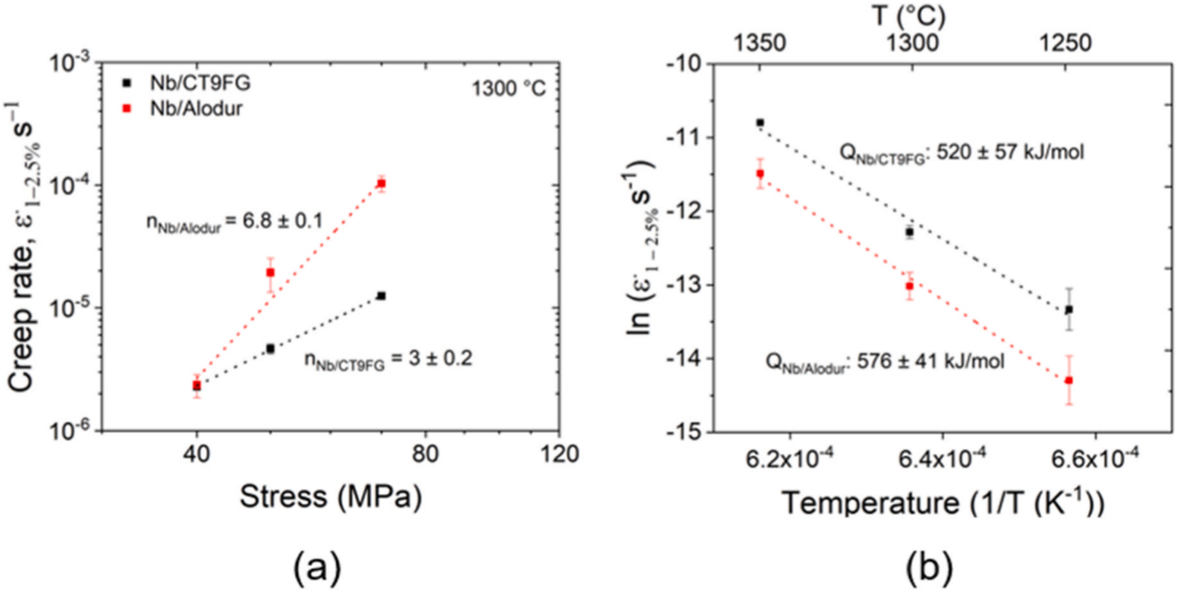

Fig. 8. Norton plots (a) and Arrhenius plots (b) obtained from creep tests conducted on Nb/CT9FG and Nb/Alodur composites for the determination of the apparent stress exponent (n_{app}) and apparent activation energy (Q_{app}).

magnification out of the marked region in Fig. 9a. The darker contrast corresponds to Al_2O_3, while the brighter contrast represents the Nb metallic phase. In general, the heavy damage in particular of the alumina phase is visible. Besides the fracture of alumina also

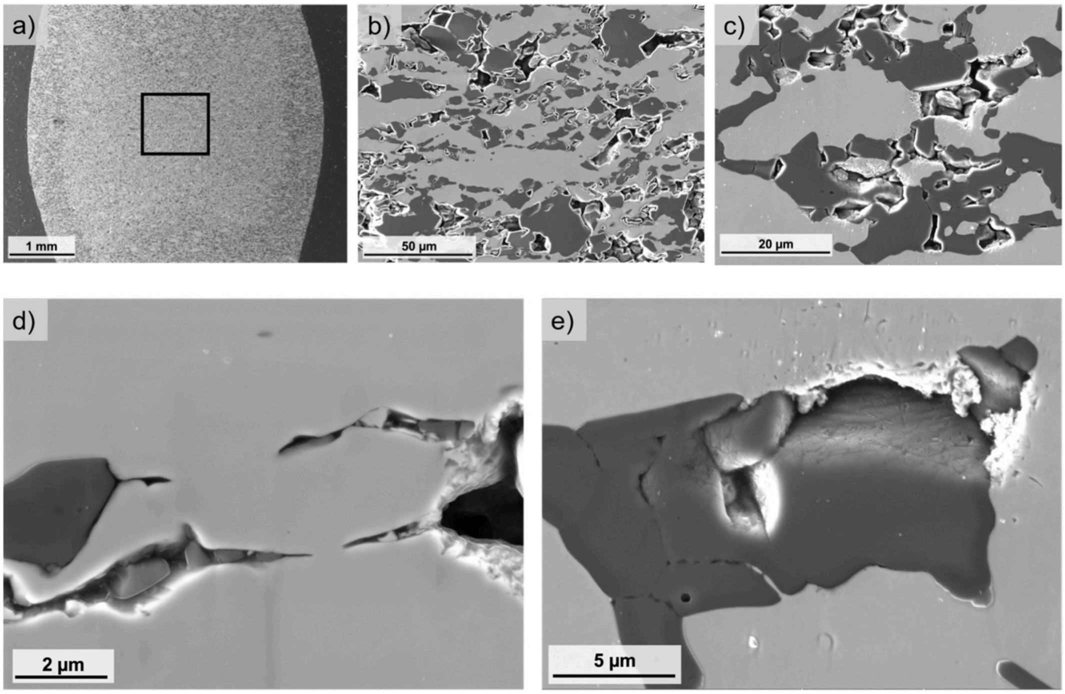

Fig. 9. SE micrographs of the 60/40 Nb/CT9FG composite after compression testing at 1300 °C, deformed to ~23% strain at a final stress of 125 MPa. (a) General overview. The marked square region is shown at higher magnification in (b, c). (b) Severe damage of alumina particles. (c) Fracture of Al_2O_3 particles accompanied by delamination at Nb/Al_2O_3 interfaces. (d) Cracks within the Nb matrix initiated from fractured or delaminated alumina particles; alumina particles directly beneath the surface are also visible. (e) Fractured alumina particle with pronounced deformation of the surrounding Nb matrix in the vicinity of the interface. The loading direction is vertical.

delamination occurred at the ceramic/metal interface. Cracks within the metallic niobium matrix were not observed at all. Rarely, cracks running from the alumina interface into the Nb matrix were observed, which are, however, closely related to underlying alumina particles (see Fig. 9d.) Heavy deformation was observed in the vicinity of alumina/Nb interfaces. This behaviour is indicative of a mismatch in mechanical properties between the ductile Nb and the brittle Al_2O_3, where the ceramic particles act as crack initiators under compressive loading. In Fig. 9e, the brittle fracture of Al_2O_3 is evident, with cracks propagating through and along the ceramic grains. The microstructure of the 60/40

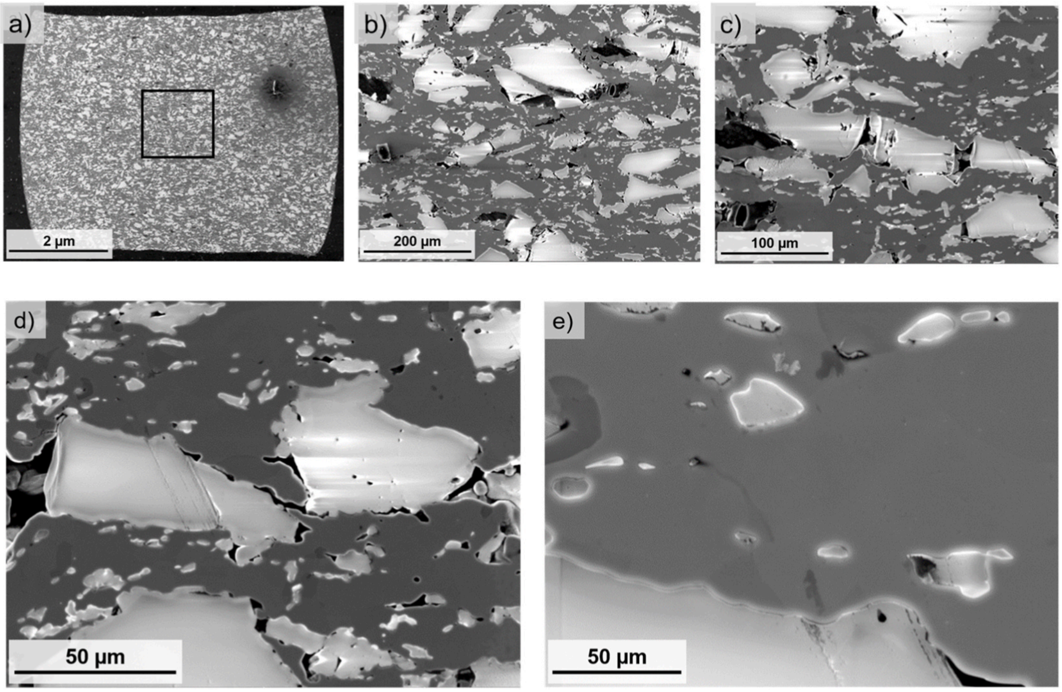

Fig. 10. SE micrographs of the 60/40 Nb/Alodur composite after a creep test at 1300 °C at an initial stress of 40 MPa and a test duration of 9 h: (a) General overview. Marked square region in (b, c) at higher magnification. (b) Fallout of small alumina particles. (c) Fracture of Al_2O_3 particles as well as delamination at Nb/Al_2O_3 interfaces. (d) Cracks within Nb starting from delaminated alumina particles. (e) Small damage features (pores) in niobium. Loading direction is vertical.

Nb/Alodur composite shows the same damage behaviour (fracture of alumina, delamination of the interface metal/ceramic) as the 60/40 Nb/CT9FG composite and is, therefore, not shown here in detail for the sake of brevity. For completeness, the corresponding micrograph is provided in the Supplementary Material (Fig. S1).

Creep. Fig. 10 gives an overview of the damage behaviour exemplarily of the 60/40 Nb/Alodur composite after creep at 1300 °C at an initial stress of 40 MPa with a duration of 9 h. Besides the larger grain size of Alodur, similar macroscopic damage behaviour was observed as in the quasi-static compression tests resulting in fracture of the alumina particles most probably along grain boundaries within large alumina particles (see Fig. 10c). Furthermore, delamination of the interface niobium/alumina was observed (Fig. 10d). Moreover, some hollow spaces are visible, which were caused most probably by fall of smaller delaminated alumina particles (see Fig. 10b). Cracks within the niobium matrix were observed very rarely caused by interconnecting delamination of alumina particles or particles directly below the specimen's surface.

Fig. 11 shows the microstructure of the same specimen presented in Fig. 10 at higher magnification captured in BSE contrast (Fig. 11a) together with the corresponding EBSD results (Fig. 11b–d) of this area.

Already the BSE micrograph reveals the formation of subgrains within the Nb grains. Considering that the average Nb grain size in the as-sintered condition was about 22 μm (see Figs. 2 and 3), regions smaller than 5 μm with distinct grey-scale contrast are most likely associated with subgrains. Fig. 11b shows the crystallographic orientation map with respect to the loading axis (vertical), whereas Fig. 11c shows the band contrast map with low angle grain boundaries (LAGBs) with a misorientation of 2° indicated in red and high angle grain boundaries (HAGBs) with a misorientation of 12° (blue lines). Thus, it turns out that two Nb grains (yellow-greenish) are located in the centre of Fig. 11b, which are separated by a HAGB (blue, centre). However, both grains contain indeed also several LAGBs (red). In addition, fine precipitates (darker grey spots) were present in the microstructure either at HAGBs and LAGBs or in the grain interior. These precipitates are niobium carbides, which have been reported for the initial niobium powder previously by Refs. [13,14,27,28].The carbides were identified by XRD as β-Nb_2C in the initial Nb powder as well as after casting followed by pressureless sintering [27–29]. Additional niobium-carbide (NbC) formation due to carbon uptake from graphite tools during FAST processing was measured also by XRD (not shown here). Carbon uptake from graphite tools is a well-recognised phenomenon in FAST processing and can occur via (i) solid-state diffusion from the die/foil into surface layers and (ii) infiltration/condensation of CO/CO_2 within open porosity, potentially leading to carbide formation and changes in measured properties [30]. In situations where phase stability is critical, it has been reported in some studies that Ta/Mo barrier foils can be used to prevent tool/specimen interactions [31,32]. However, in the present study the number of formed carbides seems to vary from batch to batch. Thus, for instance comparable precipitates were not observed in the microstructure of specimens analysed after quasi-static compression testing. Hence, within the scope of the present study, it is not straightforward to isolate and quantify a direct contribution of these precipitates to the measured mechanical response. In addition to Nb–C interactions, Eusterholz et al. have reported that at α-Al_2O_3/Nb interfaces, oxygen transport along defects may promote the formation of nanoscale Nb oxides and even the onset of ternary niobate phases (e.g., $AlNbO_4$), potentially weakening interfacial cohesion during prolonged thermal exposure [12]. However, under the experimental conditions investigated in the present work, no indications of Nb-oxide or ternary niobate formation were observed via SEM and XRD. For full clarification, additional TEM investigations would be beneficial, but are out of the scope of the present studies.

Fig. 11d shows the kernel average misorientation map in the misorientation angle range between 0° and 3°. Besides the fact that the LAGBs (red) in Fig. 11c agree well with the regions of high local misorientation it is further visible that even in the remaining larger parts of both grains first indicators for the formation of further subgrains are visible (see white arrows), however with a local misorientation lower than 2°.

4. Discussion

4.1. Influence of alumina particle size and niobium content on quasi-static compression behaviour

The difference in alumina particle size significantly affected the mechanical performance of the Nb–Al_2O_3 composites. Nb/CT9FG composites, due to their finer particle size, exhibited higher density after the FAST process, as confirmed by the relative density and porosity values in Table 2. They demonstrated higher yield strength than Nb/Alodur composites only at Nb contents of 60% and above. At lower Nb contents

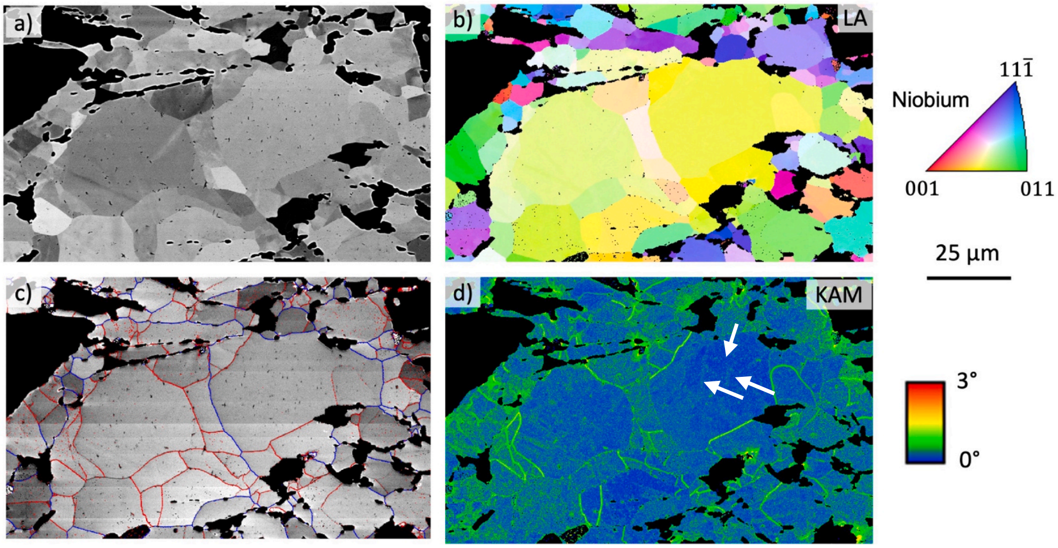

Fig. 11. (a) Micrograph of the Nb matrix in the 60/40 Nb/Alodur composite after creep testing at 1300 °C at an initial stress of 40 MPa, captured in BSE contrast. EBSD measurements of the area in (a) are shown in (b–d): (b) crystallographic orientation map with respect to the loading axis, (c) grain map, and (d) kernel average misorientation (KAM) map.

(≤40%), however, Nb/Alodur composites showed higher yield strength. This behaviour is rationalised by the structural role of coarse alumina particles, which act as a reinforcing framework constraining the metallic matrix. This effect becomes particularly evident at 60% Alodur content and above, where the formation of a continuous ceramic skeleton led to a distinct step in strength compared to the composite with 40% Alodur. As illustrated in Fig. 4c, the Nb/CT9FG composites followed a linear rule of mixture, a trend which was not observed in the Alodur-containing counterparts.

Another noteworthy result was observed in the 20/80 Nb/Alodur specimen. Unlike the other Nb/Alodur composites, which exhibited strain hardening during testing, this specimen did not display such behaviour. Instead, after reaching its maximum strength, a decrease in stress was recorded despite continued strain accumulation. The influence of the microstructure on this behaviour is evident, although different factors may have contributed to it. Firstly, as shown in Table 2, this specimen possessed the highest porosity among all tested materials. Such high porosity may have facilitated the formation of early cracks, which could account for the absence of strain hardening. In addition, with low Nb content in this composition, the continuity of the Nb phase was not achieved, resulting in a deformation response that differed from the other Nb/Alodur composites and more closely resembled the brittle fracture behaviour of ceramics. The fact that the specimen did not fail totally is likely due to the presence of Nb grains within the microstructure, albeit in a dispersed distribution.

Previous studies by the authors [13,14], demonstrated that porosity has a substantial impact on the mechanical performance of castable and extruded Nb–Al_2O_3 materials. In contrast, the FAST-processed composites investigated in the current study exhibited markedly lower porosity and, consequently, significantly higher compressive strength. These findings underscore the effectiveness of the FAST technique in fabricating dense refractory composites with good high-temperature performance under compressive loads.

4.2. *Influence of alumina particle size and niobium content on creep behaviour*

The variation in creep behaviour as a function of Nb content is shown in Fig. 6. As expected, an increase in the Nb content resulted in reduced creep resistance of the composites. This is a predictable outcome, considering that creep deformation predominantly occurs within the metallic matrix. Therefore, a higher Nb content is expected to lead to increased creep strain and higher creep rates in the composites.

At 1300 °C and an initial stress of 40 MPa, the Nb/CT9FG and Nb/Alodur composites, despite their different alumina particle sizes, exhibited similar creep curves (see Figs. 5 and 7). Both materials followed almost the same deformation path during testing and completed the 9-h creep experiments at a strain rate of approximately $2 \times 10^{-6}\ s^{-1}$, reaching about 8% strain. These findings suggest that, under identical stress and temperature conditions, the effect of alumina particle size on the overall creep response of the composites is negligible. While this observation does not entirely rule out the influence of particle size, it indicates that, within the tested conditions, creep behaviour is relatively insensitive to it.

The influence of alumina particle size became more evident when the experiments were conducted at different temperatures and stress levels, as demonstrated by the results of the Norton and Arrhenius plots (Fig. 8). The Nb/CT9FG and Nb/Alodur composites exhibited apparent stress exponents of $n_{app} = 3$ and $n_{app} = 6.8$, respectively. The stress exponent for the Nb/CT9FG composite is notably lower than that reported for pure niobium under similar testing conditions ($n \approx 7.5$) [33], but slightly higher than the typical range reported for Al_2O_3 ceramics ($n \approx 1$–2) [34–36]. This value also exceeds that typically associated with grain boundary sliding ($n \approx 2$).

In the Nb/Alodur composite, the continuity of the metallic matrix leads the material to behave predominantly like niobium during creep testing. In this system, the alumina particles act as inert inclusions, remaining rigid within the matrix while the niobium phase deforms around them. At 1300 °C, the homologous temperature of niobium is approximately 0.57 T_m, which is relatively low; therefore, niobium exhibits a high stress exponent under these conditions. The measured stress exponent of $n_{app} = 6.8$ for Nb/Alodur confirms that the composite deformation is strongly dominated by the metallic niobium phase.

By contrast, the Nb/CT9FG composite possessed a fine-grained structure. In such systems, grain boundary sliding, phase boundary sliding, or diffusion-assisted creep mechanisms may contribute to the overall deformation behaviour. However, with 60% Nb present, the material does not deform like pure Nb or pure Al_2O_3 either. Instead, it shows an intermediate stress exponent of $n_{app} \approx 3$, reflecting a concurrent deformation response of both phases. In this case, the very fine-grained alumina particles act as a skeleton, interpenetrating with the niobium skeleton and constraining creep deformation. Consequently, both the metallic and ceramic phases are forced to deform concurrently, giving truly rise to a composite creep behaviour. These findings are in agreement with previous studies investigating the influence of grain or particle size on creep behaviour [37–39].

The influence of alumina particle size was further confirmed by the experiments conducted at various temperatures. The apparent activation energies for the Nb/CT9FG and Nb/Alodur composites were calculated as 520 ± 57 and 576 ± 41 kJ/mol, respectively. Since these are multiphase materials, their creep behaviour cannot be expected to replicate that of single-phase systems. Consequently, the obtained values lie between those reported for pure Nb and polycrystalline Al_2O_3. Specifically, the activation energies are considerably higher than the self-diffusion activation energy of pure niobium, which typically ranges between 246 and 438 kJ/mol depending on crystallographic orientation, impurity content, and testing conditions [40–42]. On the other hand, they remain below the values generally reported for polycrystalline alumina, which are in the range of 626–785 kJ/mol [34,36].

5. Conclusions

In this study, the high-temperature mechanical behaviour of Nb–Al_2O_3 refractory composites fabricated via the FAST method was investigated under compressive loading. The results were comparatively analysed with respect to alumina particle size, Nb content, and other testing parameters, leading to the following key conclusions.

- The compressive strength of the composites was governed by both the Nb content and the alumina particle size. At lower Nb contents (≤40%), Alodur-reinforced composites exhibited higher yield strength and more pronounced strain hardening, whereas at higher Nb contents (≥60%), CT9FG-based composites showed higher compressive strength. Notably, the compressive behaviour of the Nb/CT9FG system followed a linear rule-of-mixture trend with increasing metal phase fraction.
- Despite showing similar creep curves under identical conditions (1300 °C, 40 MPa), the Nb/CT9FG and Nb/Alodur composites exhibited distinct differences in deformation under different stresses and temperatures. The Nb/CT9FG composite revealed an intermediate apparent stress exponent ($n_{app} \approx 3$), suggesting concurrent deformation of both phases, whereas the Nb/Alodur composite showed a higher apparent stress exponent ($n_{app} \approx 6.8$), reflecting deformation dominated by the niobium matrix.
- The apparent activation energies of both composites (520 ± 57 kJ/mol for Nb/CT9FG and 576 ± 41 kJ/mol for Nb/Alodur) fall between those of pure niobium and polycrystalline alumina. This confirms that creep behaviour is governed by the dual-phase nature of the composites, where microstructural features such as particle size, phase distribution, and interfacial interactions play a decisive role.

- Post-mortem microstructural analyses revealed subgrain formation and the presence of thermally activated precipitates within the niobium matrix, particularly after long-term creep exposure. Interface damage and alumina fracture were common in both composite types.

Overall, the findings demonstrate that optimising Nb content and alumina particle size significantly enhances the high-temperature compressive performance of Nb-Al$_2$O$_3$ composites. Moreover, the results emphasise that factors beyond porosity, such as composition, metal content and particle size, play a critical role in determining the observed the high-temperature deformation response. While the present study is focused on compressive loading conditions, complementary mechanical testing modes (e.g. tensile, bending, and fracture-related tests) would be valuable to further assess the applicability of these composites under complex service conditions.

CRediT authorship contribution statement

Gökhan Günay: Writing – original draft, Visualization, Resources, Methodology, Investigation, Formal analysis, Data curation, Conceptualization. **Gregory Kallien:** Writing – review & editing, Resources, Investigation. **Bastian Kraft:** Resources. **Susanne Wagner:** Writing – review & editing, Funding acquisition. **Karl Günter Schell:** Writing – review & editing, Funding acquisition. **Martin Heilmaier:** Writing – review & editing, Supervision. **Horst Biermann:** Writing – review & editing, Supervision, Project administration, Funding acquisition, Conceptualization. **Anja Weidner:** Writing – review & editing, Writing – original draft, Visualization, Supervision, Methodology, Investigation, Funding acquisition, Conceptualization.

Declaration of competing interest

The authors declare that they have no known competing financial interests or personal relationships that could have appeared to influence the work reported in this paper.

Acknowledgements

The authors would like to express their gratitude to Mr Thomas Ludewig for his assistance in specimen preparation, and to Dipl.-Ing. Diane Hübgen, Mrs Katrin Becker, and Mrs Birgit Witschel for their support in preparing specimens for metallographic investigations via scanning electron microscopy. Special thanks are also extended to Dr.-Ing. Florian Kerber and Dr.-Ing. Nora Brachhold for their support with platinum coating prior to EBSD measurements. The provision of cast reference specimens for comparison purposes by Dr.-Ing. Tilo Zienert and Prof. Dr.-Ing. habil. Christos G. Aneziris is gratefully acknowledged. This research was financially supported by the German Research Foundation (DFG) within the Research Unit FOR 3010 under project number 416817512.

Appendix A. Supplementary data

Supplementary data to this article can be found online at https://doi.org/10.1016/j.ceramint.2026.03.228.

References

[1] D.E. Garcia, S. Schicker, R. Janssen, N. Claussen, Nb- and Cr-Al$_2$0$_3$ composites with interpenetrating networks, J. Eur. Ceram. Soc. 18 (1998) 601–605, https://doi.org/10.1016/S0955-2219(97)00211-2.

[2] J. Mayer, C.P. Flynn, M. Rühle, High-resolution electron microscopy studies of Nb/Al$_2$O$_3$ interfaces, Ultramicroscopy 33 (1990) 51–61, https://doi.org/10.1016/0304-3991(90)90104-T.

[3] D.E. García, S. Schicker, J. Bruhn, R. Janssen, N. Claussen, Mechanical properties of pressureless-sintered niobium-alumina-matrix composites, J. Am. Ceram. Soc. 81 (1998) 429–432, https://doi.org/10.1111/j.1151-2916.1998.tb02353.x.

[4] D. Korn, G. Elssner, R.M. Cannon, M. Rühle, Fracture properties of interfacially doped Nb-A1$_2$O$_3$ bicrystals: i, fracture characteristics, Acta Mater. 50 (2002) 3881–3901, https://doi.org/10.1016/S1359-6454(02)00193-3.

[5] R.K. Kirby, T.A. Hahn, B.D. Rothrock, Thermal expansion, in: Am. Inst. Phys. Handb., third ed., McGraw-Hill Publ, New York, NY, 1972.

[6] E. del Rio, J.M. Nash, J.C. Williams, M.C. Breslin, G.S. Daehn, Co-continuous composites for high-temperature applications, TMS 2006 Mukherjee Symp. 463 (2007) 115–121, https://doi.org/10.1016/j.msea.2006.07.162.

[7] D.E. Garcia, S. Schicker, J. Bruhn, R. Janssen, N. Claussen, Synthesis of novel niobium aluminide-based composites, J. Am. Ceram. Soc. 80 (1997) 2248–2252, https://doi.org/10.1111/j.1151-2916.1997.tb03114.x.

[8] S. Schafföner, C.G. Aneziris, Pressure slip casting of coarse grain oxide ceramics, Ceram. Int. 38 (2012) 417–422, https://doi.org/10.1016/j.ceramint.2011.06.064.

[9] J. Fruhstorfer, C. Demuth, P. Goetze, C.G. Aneziris, S. Ray, U. Gross, D. Trimis, How the coarse fraction influences the microstructure and the effective thermal conductivity of alumina castables – an experimental and numerical study, J. Eur. Ceram. Soc. 38 (2018) 303–312, https://doi.org/10.1016/j.jeurceramsoc.2017.07.038.

[10] J. Fruhstorfer, C. Aneziris, The influence of the coarse fraction on the porosity of refractory castables, J. Ceram. Sci. Technol. 5 (2014) 155–166, https://doi.org/10.4416/JCST2013-00043.

[11] E. Storti, M. Neumann, T. Zienert, J. Hubálková, C.G. Aneziris, Metal-ceramic beads based on niobium and alumina produced by alginate gelation, Materials 14 (2021) 5483, https://doi.org/10.3390/ma14195483.

[12] M.K. Eusterholz, T. Boll, V. Ott, M. Stüber, Y. Lu, J. Gebauer, S. Ulrich, A. Kauffmann, M. Heilmaier, Nanoscale oxide formation at α-Al$_2$O$_3$–Nb interfaces, Adv. Eng. Mater. 25 (2023) 2201441, https://doi.org/10.1002/adem.202201441.

[13] G. Günay, T. Zienert, D. Endler, C.G. Aneziris, H. Biermann, A. Weidner, High-temperature compressive behavior of refractory alumina–niobium composite material, Adv. Eng. Mater. 24 (2022) 2200292, https://doi.org/10.1002/adem.202200292.

[14] G. Günay, T. Zienert, D. Endler, C.G. Aneziris, H. Biermann, A. Weidner, Influence of particle size and fabrication method on mechanical properties of Nb-Al$_2$O$_3$ refractory composites under compressive loads at high temperatures, Ceram. Int. (2024), https://doi.org/10.1016/j.ceramint.2024.12.391.

[15] G.F. Bocchini, The influences of porosity on the characteristics of sintered materials, SAE Trans. 95 (1986) 790–805, https://doi.org/10.4271/860148.

[16] T. Zienert, D. Endler, J. Hubálková, G. Günay, A. Weidner, H. Biermann, B. Kraft, S. Wagner, C.G. Aneziris, Synthesis of niobium-alumina composite aggregates and their application in coarse-grained refractory ceramic-metal castables, Materials 14 (2021) 6453, https://doi.org/10.3390/ma14216453.

[17] J.R. Groza, Field-activated sintering, in: ASM Handb., 1998, pp. 583–589.

[18] J.R. Groza, M. Garcia, J.A. Schneider, Surface effects in field-assisted sintering, J. Mater. Res. 16 (2001) 286–292, https://doi.org/10.1557/JMR.2001.0043.

[19] S. De la Torre Díaz, D. García, N. Claussen, R. Janssen, Y. Nishikawa, H. Miyamoto, R. Martínez-Sánchez, A. García-Luna, D. Rios-Jara, Spark plasma sintering of Alumina–Cr and –Nb composites, J. Metastable Nanocryst. Mater. 13 (2002) 299–306. https://dx.doi.org/10.4028/www.scientific.net/JMNM.13.299.

[20] R.A. Saucedo-Acuña, H. Monreal-Romero, A. Martínez-Villafañe, J.G. Chacon-Nava, U. Arce-Colunga, C. Gaona-Tiburcio, S.D. De la Torre, High temperature oxidation–sulfidation behavior of Cr–Al$_2$O$_3$ and Nb–Al$_2$O$_3$ composites densified by spark plasma sintering, Mater. Sci. Eng., A 471 (2007) 69–74, https://doi.org/10.1016/j.msea.2007.02.115.

[21] A.L.B. Dotta, F.L. Serafini, M.F.C. Ordoñez, I.F. Machado, M.C.M. Farias, Mechanical and tribological properties of spark plasma sintered Nb–Al$_2$O$_3$ composites, Ceram. Int. 47 (2021) 6800–6812, https://doi.org/10.1016/j.ceramint.2020.11.023.

[22] B. Kraft, S. Wagner, K.G. Schell, M.J. Hoffmann, Field-assisted sintering of Nb–Al$_2$O$_3$ composite materials and investigation of electrical conductivity, Adv. Eng. Mater. 24 (2022) 2200063, https://doi.org/10.1002/adem.202200063.

[23] M. Neumann, K. Michon, D. Endler, T. Zienert, H. Jelitto, G.A. Schneider, C. G. Aneziris, On the fracture behaviour of niobium–alumina castables, J. Eur. Ceram. Soc. 43 (2023) 5026–5031, https://doi.org/10.1016/j.jeurceramsoc.2023.03.027.

[24] ASM handbook committee, properties and selection: nonferrous alloys and special-purpose materials, in: ASM Handbook, ASM International, 1990, https://doi.org/10.31399/asm.hb.v02.9781627081627.

[25] Engineered materials handbook, Vol.4: Ceramics and glasses, in: ASM Handbook, ASM International, 1991.

[26] A.K. Mukherjee, J.E. Bird, J.E. Dorn, Experimental Correlations for high-temperature Creep, Lawrence Berkeley National Laboratory. LBNL, 1968. Report #: UCRL-18526, https://escholarship.org/uc/item/31p4z5v2.

[27] T. Zienert, D.K. Gunasekar, D. Endler, C. Faßauer, C.G. Aneziris, Additive manufacturing of layered Nb-Al$_2$O$_3$ composite granules based on paste extrusion, Metals 16 (2026) 101, https://doi.org/10.3390/met16010101.

[28] T. Zienert, D. Endler, J. Hubálková, P. Gehre, M. Eusterholz, T. Boll, M. Heilmaier, G. Günay, A. Weidner, H. Biermann, B. Kraft, S. Wagner, C.G. Aneziris, Coarse-grained refractory composite castables based on alumina and niobium, Adv. Eng. Mater. 24 (2022) 2200296, https://doi.org/10.1002/adem.202200296.

[29] T. Zienert, D. Endler, N. Brachhold, M. Weiner, M. Schmidtchen, U. Prahl, C. G. Aneziris, Characterization of sintered niobium–alumina refractory composite granules synthesized by castable technology, Adv. Eng. Mater. 24 (2022) 2200407, https://doi.org/10.1002/adem.202200407.

[30] K.E. Smetanina, P.V. Andreev, A.V. Nokhrin, E.A. Lantsev, V.N. Chuvildeev, Carbon contamination during spark plasma sintering of powder materials: a brief

overview, J. Alloys Compd. 973 (2024) 172823, https://doi.org/10.1016/j.jallcom.2023.172823.

[31] A. Kawalek, K. Ozhmegov, D. Garbiec, H. Dyja, A. Arbuz, Development of an alternative manufacturing technology for niobium components, Materials 17 (2024) 3093, https://doi.org/10.3390/ma17133093.

[32] M. Sakajio, G.E. Shter, M. Mann-Lahav, V. Beilin, S. Zamir, G.S. Grader, Carbon contamination prevention during spark plasma sintering, ACS Appl. Mater. Interfaces 15 (2023) 38080–38089, https://doi.org/10.1021/acsami.3c07265.

[33] A.N. Behera, R. Kapoor, A. Sarkar, J.K. Chakravartty, Hot deformation behaviour of niobium in temperature range 700–1500°C, Mater. Sci. Technol. 30 (2014) 637–644, https://doi.org/10.1179/1743284713Y.0000000387.

[34] A.H. Chokshi, J.R. Porter, High temperature mechanical properties of single phase alumina, J. Mater. Sci. 21 (1986) 705–710, https://doi.org/10.1007/BF01145544.

[35] J. Pelleg, Creep in Ceramics, 2017, https://doi.org/10.1007/978-3-319-50826-9.

[36] M. Castillo-Rodríguez, A. Muñoz, A. Domínguez-Rodríguez, Creep study on alumina and alumina/SWCNT nanocomposites, J. Eur. Ceram. Soc. 38 (2018) 5497–5502, https://doi.org/10.1016/j.jeurceramsoc.2018.08.013.

[37] M.H.N. Beshai, S.K. Habib, A.M. Yassein, G. Saad, M.M. Hasab El-Naby, Effect of SnSb particle size on creep behaviour under power law regime of Sn-10%Sb alloy, Cryst. Res. Technol. 34 (1999) 119–126, https://doi.org/10.1002/(SICI)1521-4079(199901)34:1<119::AID-CRAT119>3.0.CO, 2-1.

[38] A. Loghman, A. Askari Kashan, M. Younesi Bidgoli, A.R. Shajari, A. Ghorbanpour Arani, Effect of particle content, size and temperature on magneto-thermo-mechanical creep behavior of composite cylinders, J. Mech. Sci. Technol. 27 (2013) 1041–1051, https://doi.org/10.1007/s12206-013-0213-9.

[39] P. Kral, J. Dvorak, V. Sklenicka, T. Masuda, Z. Horita, K. Kucharova, M. Kvapilova, M. Svobodova, The effect of ultrafine-grained microstructure on creep behaviour of 9% Cr steel, Materials 11 (2018), https://doi.org/10.3390/ma11050787.

[40] T.S. Lundy, F.R. Winslow, R.E. Pawel, C.J. McHargue, Diffusion of Nb-95 and Ta-182 in niobium (Columbium), Trans. Met. Soc. AIME 233 (1 AD) (1965). https://www.osti.gov/biblio/4577525.

[41] R.E. Einziger, J.N. Mundy, H.A. Hoff, Niobium self-diffusion, Phys. Rev. B 17 (1978) 440–448, https://doi.org/10.1103/PhysRevB.17.440.

[42] R.E. Einziger, J.N. Mundy, H.A. Hoff, Self-diffusion in niobium, J. Nucl. Mater. 69–70 (1978) 523–525, https://doi.org/10.1016/0022-3115(78)90263-5.